Journal of Luminescence 284 (2025) 121290

Contents lists available at ScienceDirect

Journal of Luminescence

journal homepage: www.elsevier.com/locate/jlumin

Highly sensitive optical nanothermometry using Er^{3+}-doped GdOF nanoparticles: synthesis, characterization, and temperature sensing applications

Federica Scardaci [a], José I. Espeso [b], Diego Pérez-Francés [c], Graziella Malandrino [a], Rafael Valiente [c,*]

[a] Dipartimento di Scienze Chimiche, Università degli Studi di Catania, and INSTM UdR Catania, Viale Andrea Doria 6, 95125, Catania, Italy
[b] CITIMAC Dept., Universidad de Cantabria, Avda. de los Castros48, 39005, Santander, Spain
[c] Applied Physics Dept., Universidad de Cantabria, Avda. de los Castros 48, 39005, Santander, Spain

ARTICLE INFO

Keywords:
Optical nanothermometry
Fluorescence Intensity Ratio (FIR)
Method
Upconversion luminescence
Temperature sensing application

ABSTRACT

The synthesis and characterization of 1 mol% Er^{3+}-doped GdOF nanoparticles for use as optical nanothermometer are presented. The nanoparticles were synthesized using a microwave-assisted solvothermal method, followed by calcination at 700 °C to obtain the oxyfluoride phase. Temperature sensitivity was evaluated using the fluorescence intensity ratio (FIR) method, based on the thermally coupled $^2H_{11/2}$ and $^4S_{3/2}$ levels of Er^{3+} over the 294–423 K range. The results demonstrate a high sensitivity, with an absolute sensitivity of 3.07 $\times$ 10^{-3} K^{-1} at 423 K and a relative sensitivity of 1.25 % K^{-1} at 294 K. These competitive values position Er^{3+}-doped GdOF nanoparticles as promising candidates for temperature sensing applications in biomedicine and nanotechnology, offering advantages over other Er^{3+}-based nanothermometers in different host matrices.

1. Introduction

Temperature plays a crucial role for ensuring a satisfactory outcome in numerous industrial processes. Consequently, the design and development of devices capable of accurately monitoring the temperature has been a hot topic in recent decades [1,2]. Nowadays, temperature sensors must not only deliver fast and accurate reading but also meet the demands of the nanotechnology era requiring exceptionally compact devices. As a result, micro- and nanothermometry have become highly active research field [3].

In micro- and nano-electronics, the continuous miniaturization of components leads to electrical current flowing through in smaller and smaller sections, creating local temperature elevation and the formation of hot spots near defects that can degrade the devices [4,5]. Detecting these effects is essential to identify potential vulnerabilities and enhance device durability. Fluorescent nanoparticles offer a straightforward and quantitative approach to monitor such thermal fluctuations [6].

In contrast, the medical field has experienced the most significant advancements and applications of nanothermometers [7]. Their nanometric size makes them ideal for interaction with biological entities, such as cells and bacteria [8].

Furthermore, nanoparticles can also be used in cancer treatment to eradicate malignant cells through localized heating, achieved either by direct laser absorption or using nanoparticles that generate heat upon excitation at specific laser wavelength [9]. In these *in vivo* applications, nanothermometers play an essential role in mapping the thermal profile of the irradiated tissue, where precise temperature control is paramount [10,11].

It is worth noting that the primary advantage of optical nanothermometers, their nanometric sizes and spatial resolution, is also their main drawback. Therefore, *in-situ* indirect temperature measurement methods are necessary to solve this problem.

Optical nanothermometers used should be materials that emit light when excited by a lamp or laser. Their temperature dependence must be calibrated by monitoring changes in one or more measurable parameters such as emission lifetimes, spectral bandwidth, intensity ratios, wavelength shifts, or polarization, in response to the local temperature variations [12].

This article is part of a special issue entitled: The 60th anniversary of Prof. Luís D. Carlos published in Journal of Luminescence.

* Corresponding author.
E-mail address: rafael.valiente@unican.es (R. Valiente).

https://doi.org/10.1016/j.jlumin.2025.121290
Received 12 March 2025; Received in revised form 7 May 2025; Accepted 9 May 2025
Available online 15 May 2025

The high toxicity of luminescence quantum dots, and colloidal nanocrystals limits their applicability in biomedicine [13,14]. In contrast, rare-earth (RE^{3+})-doped inorganic nanoparticles offer superior biocompatibility and lower toxicity, along with a broad emission spectrum spanning the UV–VIS–NIR optical range [15,16]. All these features make the RE^{3+}-doped nanoparticles as one of the most promising candidates for the development of advanced optical temperature sensors.

Rare-earth doped upconversion nanoparticles (RE-UCNPs) belong to a class of photoluminescence materials, whose optical activity is known as anti-Stokes emission [17,18]. This nonlinear optical process involves the sequential or simultaneous absorption of two or more low energy photons, resulting in the emission of light with a shorter wavelength than the excitation one [19]. The upconversion (UC) luminescence of RE-UCNPs surpasses that of transition metal ions-doped counterparts due to the distinct electronic configuration of lanthanide ions, $4f^n5s^25p^66s^2$ ($n = 0$–14). With the exception of ytterbium and cerium, all RE^{3+} ions exhibit a rich array of ladder-like 4*f*-4*f* energy levels. The electrons within these levels experience minimal electron-phonon coupling due to the shielding by the outer-lying $5s^2$ and $5p^6$ orbitals. Upon the removal of $6s^2$ electrons, the 4*f* electrons become optically active, enabling transitions either within 4*f* orbitals or between 4*f* and 5*d* orbitals.

The fluorescence intensity ratio (FIR) method is widely used as a thermometric technique [20]. It relies on the intensity ratio between two thermally coupled energy levels, which are separated by a small energy gap (30-2000 cm^{-1} depending on the application temperature range) [21]. This energy difference enables thermal energy to promote electrons from the lower to the upper level. In other words, the population distribution between these two states is governed by the Boltzmann factor, making them thermally coupled [22].

Additionally, both levels share the electronic population so that the ratio of intensities between their emissions will be independent of the excitation source and fluctuations in the particle concentration, thus providing an absolute measurement and a reliable system for temperature monitoring. This method is often referred to as self-referring method [23,24].

Compared to thermometers based on transition-metal ions like Cr^{3+} (ruby) or Mn^{4+}, FIR-based thermometers using rare-earth ions are more suitable for thermometry. This is because the energy levels of RE-ions are weakly influenced by the crystal field, allowing applicability in a variety of host materials [25].

Er^{3+} ions are widely used in FIR-based luminescence nanothermometry [26,27]. Their widespread use is due to their efficient emission and the optimal energy gap (~700 cm^{-1}) between the thermally coupled $^4S_{3/2}$ and $^2H_{11/2}$ levels. This energy difference is well-suited for thermometry applications in the physiological temperature range (30–50 °C), where maximum sensitivity is achieved, as well as for industrial applications [6]. Er^{3+} ions can be incorporated into a variety of host matrices, including oxides, fluorides or oxyfluorides.

Oxyfluorides doped with rare-earths ions offer advantages due to the combined merits of the oxide and the fluoride counterparts, such as low phonon energy, a high optical band gap, weak multi-phonon interaction, excellent mechanical strength, and high thermo-chemical stability [28,29]. These host matrices offer significant advantages over conventional sulphide, nitride, and silicate host matrices in terms of reduced toxicity, lower production costs, and simpler synthesis conditions [30].

Moreover, oxyfluorides exhibit distinctive spectroscopic properties, making them an excellent platform for the luminescence of lanthanide/rare-earth elements. This is primarily attributed to the local distortions induced in the coordination polyhedron by the mixed-ligand system, which enhances the luminescent performance [31,32].

In this context, we present an innovative approach to nanothermometry using Er^{3+}-doped gadolinium oxyfluoride nanoparticles (GdOF) as the host lattice. The 1 mol% Er^{3+}-doped GdOF nanoparticles have been synthesized through calcination of the as-prepared GdF_3 nanoparticles obtained via microwave-assisted solvothermal method. X-ray diffraction (XRD) patterns and transmission electron microscopy (TEM) have been used to characterize the nanoparticle structure and shape. The functional properties of the 1 mol% Er^{3+}-doped GdOF nanoparticles have been investigated through luminescence measurements under UV irradiation and in function of temperature.

2. Material and methods

2.1. Materials

All reagents were purchased from Sigma-Aldrich and used without any further purification.

Rare earth (RE) nitrates$Gd(NO_3)_3{\cdot}6H_2O$ (99.9%), $Er(NO_3)_3{\cdot}5H_2O$ (99.9%)ammonium fluoride NH_4F (96 %), and ethylene glycol were used for 1 mol% Er^{3+}-doped GdOF nanoparticles synthesis.

2.2. Microwave-assisted synthesis of 1 mol% Er^{3+}-doped GdOF

Er^{3+}-doped GdOF nanoparticles were prepared via microwave-assisted solvothermal method (Anton-Paar Monowave 400 reactor).

Firstly, a 10 % stock solution (0.226 M) of $Er(NO_3)_3{\cdot}5H_2O$ was prepared by weighing 1 g $Er(NO_3)_3{\cdot}5H_2O$ in 10 mL ethylene glycol.

Briefly, 9.91 mmol of $Gd(NO_3)_3{\cdot}6H_2O$ and 0.5 mL (0.11 mmol, i.e. 1 mol% of the Gd content) of the Er stock solution was mixed with 10 mL of ethylene glycol. After the solution became transparent, 8 mmol of NH_4F dissolved in 10 mL of ethylene glycol was added dropwise under vigorous stirring. The solution was then stirred for another 30 min, then transferred into a 30 mL glass vial (pressure-resistant up to 30 bar) and placed inside a microwave reactor.

The reaction was carried out at 175 °C for 1.5h under continuous stirring at 600 rpm. During the process, the pressure reached approximately 18 bar, which is significantly below the 30-bar maximum pressure tolerance of the vial. The mixture was cooled down to room temperature and washed several times with water and ethanol by centrifuging (4200 rpm x 10 min). The solid was dispersed in ethanol and dried at 70 °C [33].

Later on, a calcination at 700 °C for 6h in air was carried out with a ramp of 5 °C/min, whereby the oxyfluoride phase was obtained. The overall procedure is illustrated in Fig. 1.

2.3. Characterisation

The phase composition of the sample was examined using a Bruker D8 Advance diffractometer with Cu K_α radiation operating at 40 kV and a current intensity of 25 mA.

Photoluminescence (PL) measurements were performed using an Edinburgh Instruments FLSP920 fluorimeter equipped with double monochromators for emission and excitation. Excitation sources included a continuous 450 W Xenon lamp, a pulsed 60 W Xe lamp with variable frequencies for lifetime measurements, and a 980 nm diode laser with a tunable pump power were used ($P_{max} = 5$ W). For emission detection, three distinct electrically cooled photomultiplier tubes were employed, depending on the detection spectral range.

TEM images were obtained with a JEOL JEM 1011 coupled with a high-resolution CCD camera (Gatan, Pleasanton, United States).

3. Results and discussion

The synthesis of 1 mol% Er^{3+}-doped GdOF nanoparticles involved the initial synthesis of 1 mol% Er^{3+}-GdF_3 nanoparticles via microwave-assisted solvothermal method, confirming the orthorhombic crystal structure (*Pnma* space group), followed by a high-temperature calcination step to induce phase transition. Specifically, the GdF_3 precursor was heated up to 700 °C for 6 h to ensure the complete formation of the GdOF phase; this calcination temperature was chosen to promote

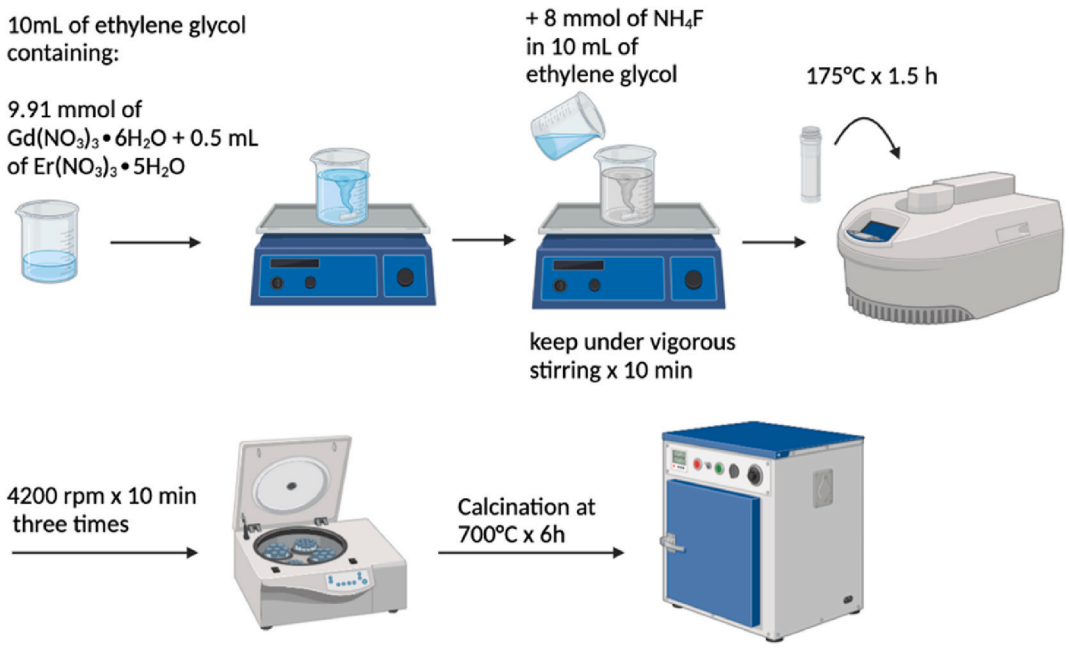

Fig. 1. Representation of the 1 mol% Er^{3+}-doped GdOF NP synthetic approach.

optimal crystallinity and phase purity.

The Rietveld refinement of the XRD pattern of Er^{3+}-doped GdOF NPs is shown in Fig. 2. The high background found in the diffractions patterns is due to Gd fluorescence. It results from the fact that gadolinium atoms emit X-rays at copper wavelength excitation.

The obtained XRD pattern clearly shows the formation of GdOF with a trigonal crystal structure ($R\bar{3}m$) according with the PDF card no.00-050-0569. The obtained lattice parameters from the refinement are $a = b = 3.8679$ (6) Å and $c = 19.253$ (2) Å with crystallite sizes of about 46 nm and strains 0.046 %. The observed peaks at 27.78°, 28.2°, 32.56°, 46.43°, 46.98° correspond to the characteristic reflection of 006, 012, 104, 018, and 110 of the GdOF phase. Additionally, small diffraction peaks of Gd_2O_3 are present (about 7 % according to the Rietveld analysis with large Bragg factor, Fig. 2), probably due to the long calcination time, corresponding to the cubic phase ($Ia\bar{3}$) and lattice parameter $a = b = c = 10.822(2)$ Å. In this case, the crystallite size is similar 53 nm while the strains are larger 0.171 %, *i.e.,* the effect of strains in the lattice parameters.

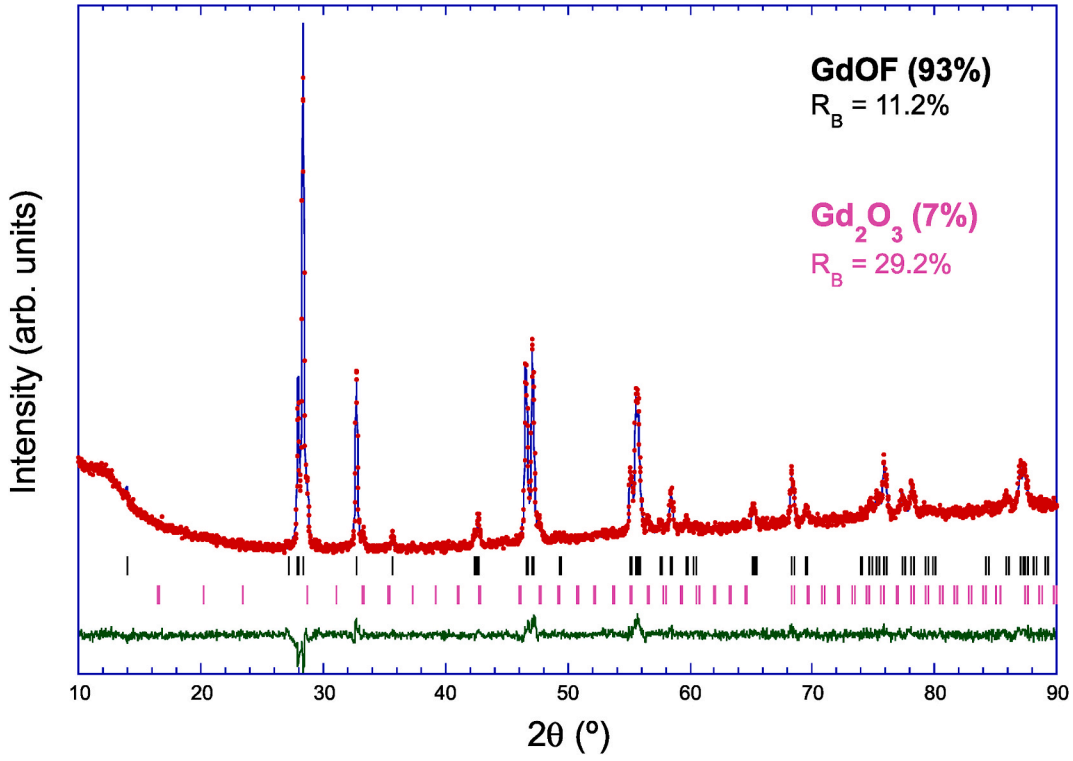

Fig. 2. XRD pattern of 1mol% Er^{3+}-doped GdOF NPs synthetized at 700 °C. Diffraction peaks from Gd_2O_3 impurities are observed (7 %). Bragg factors (R_B) are also included.

According to the literature, a pure trigonal phase of GdOF is formed at 500 °C and remained stable up to 700 °C, with enhanced crystallinity as the temperature increases [34]. However, at temperatures higher than 700 °C, impurity peaks corresponding to the cubic Gd_2O_3 (space group $Ia\bar{3}$) begin to appear in the XRD patterns. These peaks observed at 28.46°, 47.64°, 56.46° correspond to the 222, 440, and 622 reflections of the Gd_2O_3 phase, indicating that the partial decomposition of GdOF is likely caused by fluorine loss at elevated temperatures.

Although GdOF can form at lower temperatures, higher calcination temperatures help to eliminate residual fluorides. Additionally, elevated temperatures facilitate a more complete phase transition, favouring oxygen diffusion, promoting better crystallinity and improving structural stability. These factors contribute to better thermomechanical properties, making the material more suitable for advanced applications [35,36].

The morphological characterization of the Er^{3+}-doped GdOF NPs has been conducted through TEM analysis, as shown in Fig. 3. The NPs exhibit a rice-shaped morphology, with an average size in the long dimension being about 19 ± 7 nm and that in the short dimension being about 9.5 ± 2.0 nm, obtained fitting the data to a log-normal distribution function (see insets Fig. 3). While TEM images typically probe a limited number of well-dispersed nanoparticles, X-ray measurements provide an average size based on a much larger population. As a result, TEM offers detailed morphological information on individual particles but may not be fully representative of the overall sample, whereas X-ray diffraction yield statistically robust size distributions but lack spatial resolution. Therefore, combining both methods allows for a more comprehensive and reliable characterization of nanoparticle size and dispersion.

For the luminescent characterization, initial laser-based measurements were performed to identify the characteristic emissions of the nanoparticles, particularly those arising from Er^{3+} ions.

A 980 nm laser diode, with variable output pump power from 65 mW to 1186 mW, was used as the excitation source to measure the emission in the visible range, between 500 and 580 nm. The upconversion-induced luminescence exhibits two group of peaks in the green region, assigned to the $^2H_{11/2} \rightarrow {}^4I_{15/2}$ and $^4S_{3/2} \rightarrow {}^4I_{15/2}$ transitions, as illustrated in Fig. 4. As the laser power increases, the first green emission ($^2H_{11/2} \rightarrow {}^4I_{15/2}$) becomes more intense. This enhancement results from the increased population of the $^2H_{11/2}$ state at high pump power, which happens as a result of the sample heating induced by the pump power increases. The log-log plot of the green upconversion emission intensity as a function of pump power ($I \propto P^n$) shows a linear fitting with a slope of $n \approx 1.4$, which is intermediated between the case of small ($n = 2$) and large upconversion rates ($n \approx 1$) [37]. Indeed, it depends on the pump power density.

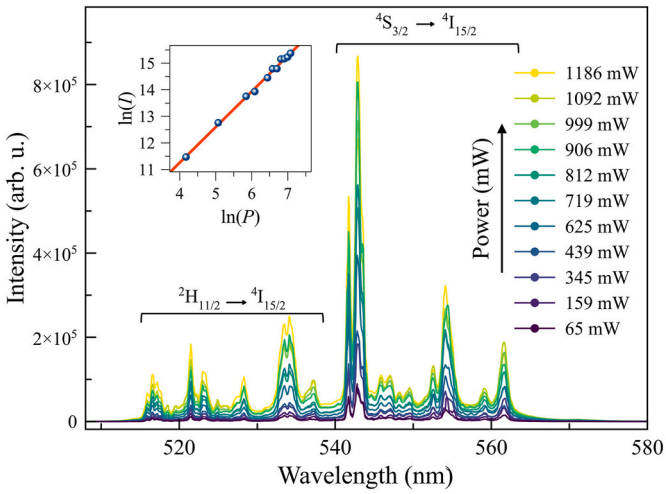

Fig. 4. Normalized UC emission spectra of 1 % Er-doped GdOF NPs ($R\bar{3}m$ space group) excited at 980 nm with different output power. The inset shows log-log plot of the UC emission intensity vs. incident pump power.

The main advantage of NIR Er^{3+} excitation over UV or Vis light is its ability to minimize photodamage, scattering and autofluorescence in biological tissues. Moreover, affordable 980 nm laser diodes enable deeper tissues penetration compared to UV–Vis sources. The excitation efficiently populates $^2H_{11/2}$ and $^4S_{3/2}$ levels of Er^{3+}, while reducing non-radiative losses, such as multiphonon relaxation. As a results, it enhances the reliability of temperature measurements, making 980 nm excitation highly effective for thermal sensing.

To understand the luminescence phenomena, the energy level diagram of Er^{3+} ions, with the approximated wavelengths associated with different transitions, is shown in the inset of Fig. 4.

Er^{3+}-doped GdOF nanoparticles have undergone a fluorescence study at various temperatures in order to evaluate their potential as efficient nanothermometers (Fig. 5). shows the photoluminescence spectra of 1 mol% Er^{3+}-doped GdOF nanoparticles in the green spectral region as a function of temperature (294–423 K), under 375.7 nm excitation wavelength. No noticeable shifts in the peak positions were observed with increasing temperature. However, the intensity ratio between emission peaks increased, indicating a temperature-dependent behaviour that can be used for thermometric applications. Er^{3+} upconversion luminescence depends on concentration, with GSA/ESA dominating below 0.2 %, while GSA/ETU becomes significant at 1 % or higher, enhancing efficiency. However, excessive Er^{3+} concentrations

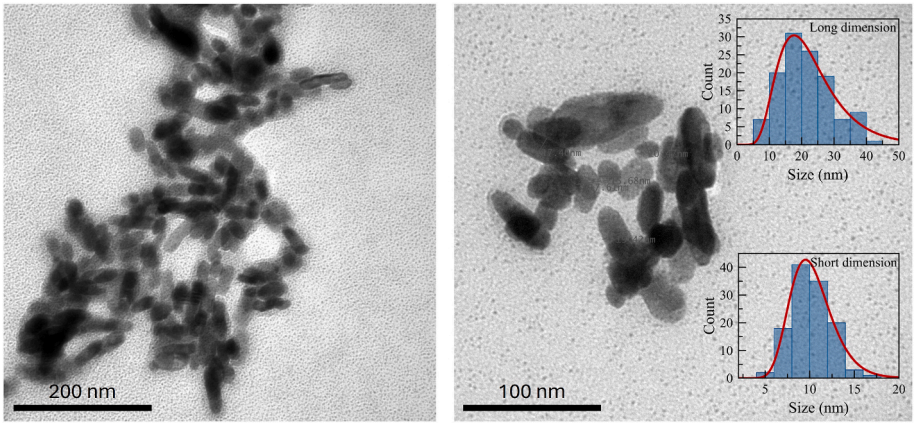

Fig. 3. TEM images and the corresponding histograms showing size distribution of 1 % Er^{3+}-doped GdOF NPs. Histograms were obtained measuring more than 120 nanoparticles (long and short distances). The red line represents the fitting to a log-normal distribution function. (For interpretation of the references to colour in this figure legend, the reader is referred to the Web version of this article.)

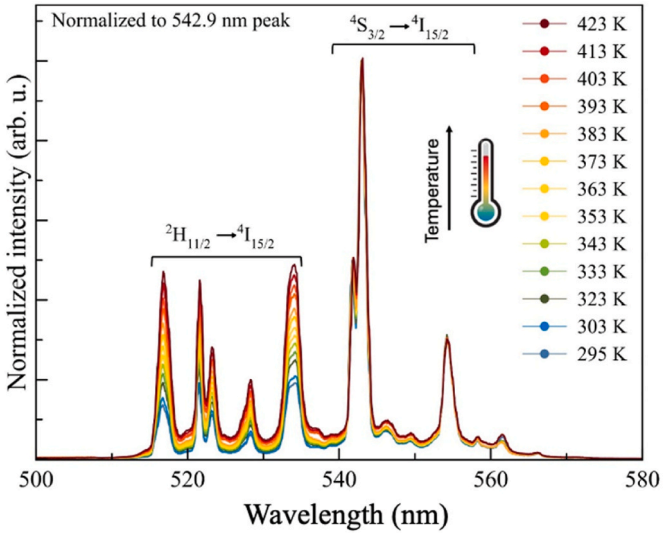

Fig. 5. Normalized emission spectra of 1 % Er^{3+}-doped GdOF NPs under λ = 375.7 nm excitation.

lead to non-radiative quenching and ion clustering, reducing luminescence and altering emission ratios. To balance strong luminescence and minimal quenching, we select 1 % Er^{3+}, a widely used standard in similar studies. This choice ensures reliable comparisons with literature and supports thermometric applications.

The emission spectra observed in Figs. 4 and 5, including peak positions, crystal-field splittings, and linewidths, confirm that the detected Er^{3+} emission originates from GdOF, when we compare our results with GdOF and Gd_2O_3 published elsewhere [32] and no fingerprints of the Er^{3+} doped Gd_2O_3 are present either after excitation at 375 or 980 nm.

The green emission consists of several peaks between 515 and 570 nm, corresponding to transitions from $^2H_{11/2}$ and $^4S_{3/2}$ excited states to the $^4I_{15/2}$ ground state of Er^{3+} [38]. Since these two excited states are thermally coupled, their emission intensity ratio, FIR, depends on the respective excited-state equilibrium populations, which are governed by the Boltzmann distribution:

$$FIR = \frac{I_{534}}{I_{543}} = C \cdot e^{-\frac{\Delta E}{kT}} \quad \text{Eq. (1)}$$

where I_{534} and I_{543} denote the integrated intensities of the emissions from the two thermally coupled multiplets to the ground state. C is a constant that depends on factors such as state degeneracy, transition probabilities, spontaneous emission rate, and photon energy of the emitting states in the host material. ΔE is the energy gap between the $^2H_{11/2}$ and $^4S_{3/2}$ multiplets. Both C and ΔE are characteristics of each material host, k is the Boltzmann constant, and T is the absolute temperature [39].

The temperature dependence of FIR can be obtained by fitting the experimental ln(*FIR*) vs. $\frac{1}{T}$ data to a linear equation, where the slope gives $\frac{\Delta E}{k}$ and the intercept, $ln(C)$, as shown in Fig. 6a). The obtained values are $\Delta E = (1082 \pm 20)\ K = 752 \pm 14\ cm^{-1}$ and $C = 6.55 \pm 0.06$. Although the energy difference (ΔE) derived from the slope values was slightly higher than the actual value, it is deemed to be acceptable.

The potential of a material for temperature sensing applications is evaluated through the absolute and relative changes in the *FIR* with temperature [40].The absolute sensitivity (S) is given by the partial derivative:

$$S = \left|\frac{\partial FIR}{\partial T}\right| = FIR\frac{\Delta E}{kT^2} \quad \text{Eq.(2)}$$

The relative sensitivity (S_R) is given by:

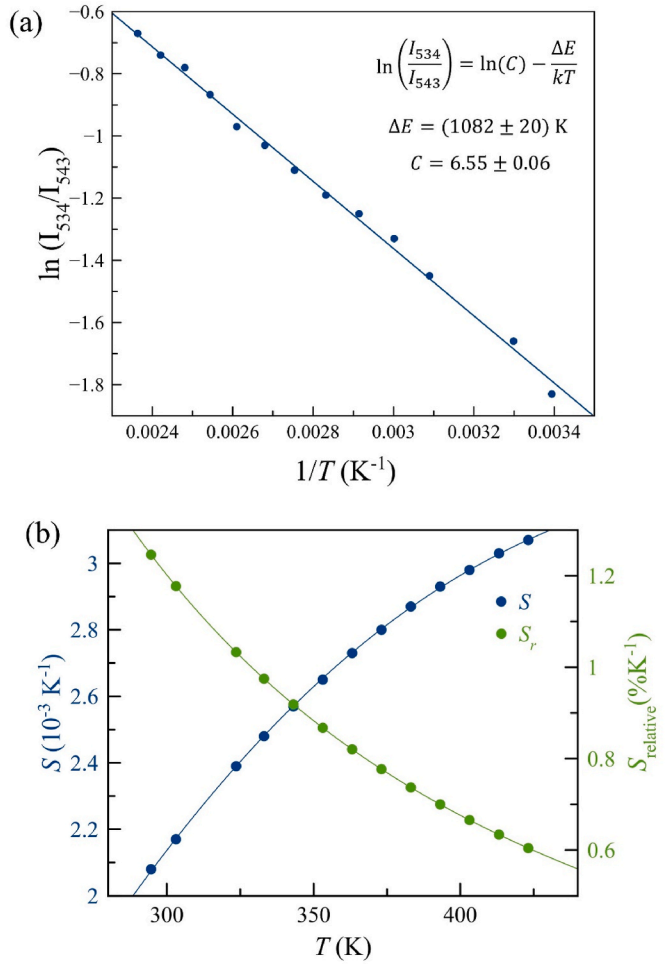

Fig. 6. (a) Semi-log plot of the FIR as a function of the reciprocal of absolute temperature, (b) absolute and relative sensitivities as function of temperature.

$$S_R = \left|\frac{1}{FIR}\cdot\frac{\partial FIR}{\partial T}\right| \times 100 = \frac{\Delta E}{kT^2} \times 100 \quad \text{Eq. (3)}$$

The obtained values for 1mol% Er^{3+}-doped GdOF nanoparticles are shown in Fig. 6 b) as a function of temperature. The highest sensitivity is found at $T = 423$ K with $S = 3.07 \times 10^{-3}\ K^{-1}$, while the highest relative sensitivity is at $T = 294$ K $(S_R = 1.25\%\ K^{-1})$, which gradually decreases with increasing temperature, reaching a value of 0.64% K^{-1} at 413 K.

These performances are highly competitive when compared to other well-stablished Er^{3+}-based optical thermometers across various host lattices. Table 1 compares the relative sensitivity (S_R) of Er^{3+}-doped GdOF nanoparticles, used as nanothermometers, with those of other hosts reported in the literature, primarily oxides and fluorides, preferably with Er^{3+} concentrations close to 1 %. It includes the calibration temperature range. As shown, the S_R of the title compound surpasses that of several previously proposed systems, confirming the potential of GdOF material as an excellent Er^{3+} host material for nanothermometric applications.

4. Conclusions

In this work, we synthesized and characterized 1 mol% Er^{3+}-doped GdOF nanoparticles via microwave-assisted solvothermal synthesis. The as-prepared GdF_3 nanoparticles (*Pnma*) underwent thermal treatment at 700 °C for 6h, enhancing crystallinity and removing fluoride phase impurities. XRD confirmed phase transformation to GdOF with a trigonal structure (*R3m*), with minor traces of Gd_2O_3 due to fluorine loss

Table 1
Summarised performance of Er^{3+} and Er^{3+}/Yb^{3+}co-doped optical nanothermometer proposed in the literature.

Host	S_R (% K^{-1}) at 335 K	Temperature range (K)	Reference
GdOF (NPs)	0.964	294 – 423	This work
$LaGdO_3$ (NPs)	0.939	298 – 873	[41]
Gd_2O_3 (NPs)	0.665	300 – 900	[42]
AlN (NPs)	0.974	300 – 470	[43]
Y_2O_3 (NPs)	1.17	293 – 490	[44]
YAG (NPs)	0.713	298 – 573	[45]
$Bi_5TiNbWO_{15}$	0.819	175 – 550	[46]
Silicate (glass)	0.528	296 – 793	[47]
SrF_2: Er^{3+}	0.885	273 – 373	[48]
CaF_2:Er^{3+} (A center)	0.949	299 – 433	[49]
CaF_2:Er^{3+} (B center)	1.039	299 – 433	[50]
KYb_2F_7:Er^{3+}	0.872	225 – 525	[51]
KGd_3F_{10}:Er^{3+},Yb^{3+}	0.955	300 – 350	[51]
β-$NaYF_4$:Er^{3+},Yb^{3+}	1.081	295 – 325	[52]
KY_3F_{10}:Er^{3+},Yb^{3+}	1.058	298 – 373	[6]
YF_3:Er^{3+},Yb^{3+}	1.006	298 – 373	[6]

at high temperature.

We demonstrated that 1 mol% Er^{3+}-doped GdOF nanoparticles are effective for nanothermometry. Using the fluorescence intensity ratio (FIR) method, we calibrated the thermalized green emissions ($^2H_{11/2}$, $^4S_{3/2} \rightarrow {}^4I_{15/2}$) over the 294–423 K temperature range. Sensitivity measurements confirmed that these nanoparticles are highly competitive for nanothermal applications. Due to their low toxicity, good thermal stability up to 600 °C, temperature above which it transforms into Gd_2O_3 in air, GdOF nanoparticles are promising candidates for biological and nanotechnological temperature-sensing, across a wide temperature range.

CRediT authorship contribution statement

Federica Scardaci: Writing – original draft, Investigation, Formal analysis. **José I. Espeso:** Writing – review & editing, Formal analysis, Data curation. **Diego Pérez-Francés:** Writing – review & editing, Validation, Investigation, Formal analysis, Data curation. **Graziella Malandrino:** Writing – review & editing, Validation, Supervision, Resources, Investigation, Funding acquisition, Conceptualization. **Rafael Valiente:** Writing – review & editing, Supervision, Project administration, Methodology, Investigation, Funding acquisition, Conceptualization.

Declaration of competing interest

The authors declare that they have no known competing financial interests or personal relationships that could have appeared to influence the work reported in this paper.

Acknowledgements

This work was partially supported by MICIU/AEI /10.13039/501100011033 and FEDER, UE through the projects PID2021-127656NB-I00 and PID2024 158839NB-I00. Additional support was received from University of Cantabria (Project P254). F.S. and G.M. thank the University of Catania within the PIA.CE.RI. 2024-2026 Linea 1 MIRACOLE project and the Erasmus+ Study program (KA131).

Data availability

Data will be made available on request.

References

[1] Carlos D.S. Brites, Patrícia P. Lima, Nuno J.O. Silva, Ángel Millán, Vítor S. Amaral, Fernando Palacio, Carlos Luis Dias, Thermometry at the nanoscale, Nanoscale 4 16 (2015) 4799–4829, https://doi.org/10.1039/c2nr30663h.
[2] Y. Chen, et al., Real-time ratiometric optical nanoscale thermometry, ACS Nano 17 (3) (Feb. 2023) 2725–2736, https://doi.org/10.1021/acsnano.2c10974.
[3] Optical nanothermometer based on the calibration of the Stokes and upconverted green emissions of Er^{3+} ions in $Y_3Ga_5O_{12}$ nano-garnet".
[4] D. Jaque, F. Vetrone, Luminescence nanothermometry, Nanoscale 4 (15) (2012) 4301, https://doi.org/10.1039/c2nr30764b.
[5] O. Zohar, M. Ikeda, H. Shinagawa, H. Inoue, H. Nakamura, D. Elbaum, D.L. Alkon, T. Yoshioka, Thermal imaging of receptor-activated heat production in single cells, Biophys. J. (1998), https://doi.org/10.1016/S0006-3495(98)77769-0.
[6] A. Assy, et al., Nanoscale thermometry with fluorescent yttrium-based Er/Yb-doped fluoride nanocrystals, Sensor Actuator Phys. 250 (Oct. 2016) 71–77, https://doi.org/10.1016/j.sna.2016.09.015.
[7] D. Jaque, B.D. Rosal, E.M. Rodríguez, L.M. Maestro, P. Haro-González, J.G. Solé, Fluorescent nanothermometers for intracellular thermal sensing, Nanomedicine 9 (7) (May 2014) 1047–1062, https://doi.org/10.2217/nnm.14.59.
[8] M. Liu, Y. Sun, D.B.L. Teh, Y. Zhang, D. Cao, Q. Mei, Nanothermometry for cellular temperature monitoring and disease diagnostics, Interdisciplinary Medicine 2 (2) (Apr. 2024) e20230059, https://doi.org/10.1002/INMD.20230059.
[9] R. López-Méndez, et al., X-Ray nanothermometry of nanoparticles in tumor-mimicking tissues under photothermia, Adv Healthcare Materials 12 (31) (Dec. 2023) 2301863, https://doi.org/10.1002/adhm.202301863.
[10] A. Bednarkiewicz, L. Marciniak, L.D. Carlos, D. Jaque, Standardizing luminescence nanothermometry for biomedical applications, Nanoscale 12 (27) (2020) 14405–14421, https://doi.org/10.1039/D0NR03568H.
[11] Xiaohua Huang, et al., Determination of the minimum temperature required for selective photothermal destruction of cancer cells with the use of immunotargeted gold nanoparticles, Photochem. Photobiol. 82 (2) (2006) 412–417.
[12] S. Ghaderi, B. Ramesh, A.M. Seifalian, Fluorescence nanoparticles 'quantum dots' as drug delivery system and their toxicity: a review, J. Drug Target. 19 (7) (Aug. 2011) 475–486, https://doi.org/10.3109/1061186X.2010.526227.
[13] M. Bottrill, M. Green, Some aspects of quantum dot toxicity, Chem. Commun. 47 (25) (2011) 7039, https://doi.org/10.1039/c1cc10692a.
[14] H. Sun, F. Zhang, H. Wei, B. Yang, The effects of composition and surface chemistry on the toxicity of quantum dots, J. Mater. Chem. B 1 (47) (2013) 6485, https://doi.org/10.1039/c3tb21151g.
[15] Z. Yu, et al., Rare-earth-metal (Nd^{3+}, Ce^{3+} and Gd^{3+})-doped CaF_2: nanoparticles for multimodal imaging in biomedical applications, Pharmaceutics 14 (12) (Dec. 2022) 2796, https://doi.org/10.3390/pharmaceutics14122796.
[16] M. Tan, G. Chen, Rare earth-doped nanoparticles for advanced in vivo near infrared imaging, in: A. Benayas, E. Hemmer, G. Hong, D. Jaque (Eds.), Near Infrared-Emitting Nanoparticles for Biomedical Applications, Springer International Publishing, Cham, 2020, pp. 63–81, https://doi.org/10.1007/978-3-030-32036-2_4.
[17] D.R. Gamelin, H.U. Gudel, Upconversion processes in transition metal and rare earth metal systems, in: H. Yersin (Ed.), Transition Metal and Rare Earth Compounds, Topics in Current Chemistry, vol.214, Springer, Berlin, Heidelberg, 2001, https://doi.org/10.1007/3-540-44474-2_1.
[18] F. Auzel, Upconversion and anti-Stokes processes with f and d ions in solids, Chem. Rev. 104 (1) (Jan. 2004) 139–174, https://doi.org/10.1021/cr020357g.
[19] I. Dinić, et al., Temperature sensing properties of biocompatible Yb/Er-doped GdF3 and YF_3 mesocrystals, J. Forensic Biomech. 15 (1) (Dec. 2023) 6, https://doi.org/10.3390/jfb15010006.
[20] M. Runowski, P. Woźny, N. Stopikowska, I.R. Martín, V. Lavín, S. Lis, Luminescent nanothermometer operating at very high temperature—sensing up to 1000 K with upconverting nanoparticles (Yb^{3+}/Tm^{3+}), ACS Appl. Mater. Interfaces 12 (39) (Sep. 2020) 43933–43941, https://doi.org/10.1021/acsami.0c13011.
[21] Y. Qin, F. Han, P. Yan, Y. Wang, Y. Zhang, S. Zhang, Fluorescence intensity ratio (FIR) analysis of the temperature sensing properties in transparent ferroelectric PMN-PT:Pr^{3+} ceramic, Ceram. Int. 47 (17) (Sep. 2021) 24092–24097, https://doi.org/10.1016/j.ceramint.2021.05.119.
[22] H. Cristina Vasconcelos, Fundamental concerns of optical fluorescence intensity ratio-based thermometry, in: A.M. Maghraby (Ed.), Luminescence - Basic Concepts and Emerging New Applications, IntechOpen, 2024, https://doi.org/10.5772/intechopen.1005917.
[23] M. Quintanilla, L.M. Liz-Marzán, Guiding rules for selecting a nanothermometer, Nano Today 19 (Apr. 2018) 126–145, https://doi.org/10.1016/j.nantod.2018.02.012.
[24] M.D. Dramicanin, Trends in luminescence thermometry, J. Appl. Phys. 128 (2020) 40902 [CrossRef]".
[25] D.D. Ragan, R. Gustavsen, D. Schiferl, Calibration of the ruby R1 and R2 fluorescence shifts as a function of temperature from 0 to 600 K, J. Appl. Phys. 72 (1992) 5539–5544.
[26] A. Ćirić, T. Gavrilović, M.D. Dramićanin, Luminescence intensity ratio thermometry with Er^{3+}: performance overview, Crystals 11 (2) (Feb. 2021) 189, https://doi.org/10.3390/cryst11020189.
[27] J. Perisa, et al., All near-infrared multiparametric luminescence thermometry using Er^{3+}, Yb^{3+}-doped YAG nanoparticles, RSC Adv. 11 (2021) 15933–15942, https://doi.org/10.1039/D1RA01647D.
[28] Y. Wei, L. Zhong, D. Li, Q. Ma, X. Dong, A novel strategy of fabricating GdOF:Er^{3+} nanofibers possessing upconversion luminescence and paramagnetic properties:

the combination of electrospinning with fluoro-oxidation technique, Opt. Mater. 95 (Sep. 2019) 109261, https://doi.org/10.1016/j.optmat.2019.109261.
[29] D. González-Mancebo, et al., Neodymium doped lanthanide fluoride nanoparticles as contrast agents for luminescent bioimaging and X-ray computed tomography, Bol. Soc. Espanola Ceram. Vidr. 61 (2022) S40–S49, https://doi.org/10.1016/j.bsecv.2021.07.004.
[30] P. Ranjith, S. Sreevalsa, Jyoti Tyagi, K. Jayanthi, G. Jagannath, Pritha Patra, Shahzad Ahmad, K. Annapurna, Amarnath R. Allu, Subrata Das, Elucidating the structure and optimising the photoluminescence properties of $Sr_2Al_3O_6F$: Eu^{3+} oxyfluorides for cool white-LEDs, J. Alloys Compd. 826 (2020), https://doi.org/10.1016/j.jallcom.2020.154015.
[31] J.S. Revathy, M. Abraham, G. Jagannath, D.N. Rajendran, S. Das, Microwave-assisted synthesis of GdOF: Eu3+/Tb3+ ultrafine phosphor powders suitable for advanced forensic and security ink applications, J. Colloid Interface Sci. 641 (Jul. 2023) 1014–1032, https://doi.org/10.1016/j.jcis.2023.03.082.
[32] T. Passuello, et al., NIR-to-visible and NIR-to-NIR upconversion in lanthanide doped nanocrystalline GdOF with trigonal structure, Opt. Mater. 33 (10) (Aug. 2011) 1500–1505, https://doi.org/10.1016/j.optmat.2011.02.029.
[33] X. Xie, et al., Suppressing the visible luminescence in GdF3:ErF3 nanoparticles with intermediate magnetic fields, J. Lumin. 239 (Nov. 2021) 118353, https://doi.org/10.1016/j.jlumin.2021.118353.
[34] J.S. Revathy, et al., Correlated structural and optical properties of crystal-engineered Eu^{3+}-doped gadolinium oxyfluoride polymorphs compatible for lighting and display applications, Ceram. Int. 50 (4) (Feb. 2024) 6769–6783, https://doi.org/10.1016/j.ceramint.2023.12.019.
[35] Y. Zhu, et al., Fine-tuning of multiple upconversion emissions by controlling the crystal phase and morphology between GdF_3 :Yb^{3+}, Tm^{3+} and GdOF:Yb^{3+}, Tm^{3+} nanocrystals, RSC Adv. 7 (5) (2017) 2426–2434, https://doi.org/10.1039/C6RA27024G.
[36] Y. Zhang, et al., Highly uniform and monodisperse GdOF:Ln3+ (Ln = Eu, Tb, Tm, Dy, Ho, Sm) microspheres: hydrothermal synthesis and tunable-luminescence properties, Dalton Trans. 42 (39) (2013) 14140, https://doi.org/10.1039/c3dt51576a.
[37] M. Pollnau, D.R. Gamelin, S.R. Lüthi, H.U. Güdel, Power dependence of upconversion luminescence in lanthanide and transition-metal-ion systems, Phys. Rev. B 61 (2000) 3337, https://doi.org/10.1103/PhysRevB.61.3337.
[38] M.A. Hernández-Rodríguez, A. Egaña, U.R. Rodríguez-Mendoza, V. Lavín, J. E. Muñoz-Santiuste, Optical temperature sensor capabilities of the green upconverted luminescence of Er3+ in La3NbO7 ceramic powders, Crystals 12 (4) (Mar. 2022) 455, https://doi.org/10.3390/cryst12040455.
[39] L.P. Qian, L.H. Zhou, H.-P. Too, G.-M. Chow, Gold decorated NaYF4:Yb,Er/NaYF4/silica (core/shell/shell) upconversion nanoparticles for photothermal destruction of BE(2)-C neuroblastoma cells, J Nanopart Res 13 (2011) 499–510.
[40] Y. Zhou, L. Li, F. Qin, Z. Zhang, Stably and highly sensitive FIR thermometry over a wide temperature range of 303-753 K based on the $GdVO_4$:Eu^{3+} and Al_2O_3:Cr^{3+} hybrid particles, Opt. Express 28 (10) (May 2020) 14366, https://doi.org/10.1364/OE.393115.
[41] V. Gutiérrez-Cano, R. Valiente, J.A. González, F. Rodríguez, High Pressure optical nanothermometer based on Er^{3+} photoluminescence, J. Phys.: Conf. Ser. 1609 (1) (Aug. 2020) 012004, https://doi.org/10.1088/1742-6596/1609/1/012004.
[42] S.K. Singh, K. Kumar, S.B. Rai, Er3+/Yb3+ codoped Gd2O3 nano-phosphor for optical thermometry, Sensor Actuator Phys. 149 (1) (Jan. 2009) 16–20, https://doi.org/10.1016/j.sna.2008.09.019.
[43] S.G. Pandya, M.E. Kordesch, Erbium doped aluminum nitride nanoparticles for nano-thermometer applications, Mater. Res. Express 2 (6) (Jun. 2015) 065006, https://doi.org/10.1088/2053-1591/2/6/065006.
[44] A.C. Brandão-Silva, et al., Size influence on temperature sensing of erbium-doped yttrium oxide nanocrystals exploiting thermally coupled and uncoupled levels' pairs, J. Alloys Compd. 731 (Jan. 2018) 478–488, https://doi.org/10.1016/j.jallcom.2017.09.156.
[45] G. Liu, et al., Investigation into the temperature sensing behavior of Yb^{3+} sensitized Er^{3+} doped Y_2O_3 , YAG and $LaAlO_3$ phosphors, RSC Adv. 5 (64) (2015) 51820–51827, https://doi.org/10.1039/C5RA05986K.
[46] H. Zou, X. Wang, Y. Hu, X. Zhu, Y. Sui, Z. Song, Optical temperature sensing by upconversion luminescence of Er doped Bi5TiNbWO15ferroelectric materials, AIP Adv. 4 (12) (Dec. 2014) 127157, https://doi.org/10.1063/1.4905454.
[47] C. Li, B. Dong, S. Li, C. Song, Er3+–Yb3+ co-doped silicate glass for optical temperature sensor, Chem. Phys. Lett. 443 (4–6) (Aug. 2007) 426–429, https://doi.org/10.1016/j.cplett.2007.06.081.
[48] S. Ryszczyńska, K. Trejgis, Ł. Marciniak, T. Grzyb, Upconverting SrF_2 :Er^{3+} nanoparticles for optical temperature sensors, ACS Appl. Nano Mater. 4 (10) (Oct. 2021) 10438–10448, https://doi.org/10.1021/acsanm.1c01964.
[49] J.A. Sanz-García, G. Lifante-Pedrola, J.E.M. Santiuste, E. Cantelar, Dual luminescent nano-thermometry based on the selective excitation of optical centers in CaF2:Er3+ nanoparticles, J. Alloys Compd. 1010 (Jan. 2025) 177529, https://doi.org/10.1016/j.jallcom.2024.177529.
[50] S. Su, et al., KYb_2F_7 :Er^{3+} based nanothermometers: controlled synthesis, enhanced red emission, and improved sensitivities via crystal-site engineering, J. Mater. Chem. C 11 (6) (2023) 2375–2388, https://doi.org/10.1039/D2TC04121A.
[51] K. De Oliveira Lima, L.F. Dos Santos, R. Galvão, A.C. Tedesco, L. De Souza Menezes, R.R. Gonçalves, Single Er3+, Yb3+: KGd3F10 nanoparticles for nanothermometry, Front. Chem. 9 (Jul. 2021) 712659, https://doi.org/10.3389/fchem.2021.712659.
[52] I.M. Gonçalves, A.R. Pessoa, C. Hazra, Y.S. Correales, S.J.L. Ribeiro, L. De S. Menezes, Phonon-assisted NIR-to-visible upconversion in single β-NaYF4 microcrystals codoped with Er3+ and Yb3+ for microthermometry applications: experiment and theory, J. Lumin. 231 (Mar. 2021) 117801, https://doi.org/10.1016/j.jlumin.2020.117801.